JOURNAL OF AIRCRAFT
Vol. 42, No. 4, July-August 2005

Wake-Vortex Alleviation Flowfield Studies

Donald A. Durston,[*] Stephen M. Walker,[†] David M. Driver,[‡] and Stephen C. Smith[§]
NASA Ames Research Center, Moffett Field, California 94035-1000
and
Ömer Savaş[¶]
University of California, Berkeley, Berkeley, California 94720-1740

Wake-vortex-alleviation research was conducted in the far-field vortex wake of a generic wing-tail aircraft model. The goals were to achieve accelerated vortex strength reduction and to map the conditions at which this reduction would occur. The wing-tail model was run in a water tow tank to generate a pair of unequal-strength counter-rotating vortices on each side of centerline. Dye flow visualization provided physical insight into the nature of the vortex interactions, and three-component particle image velocimetry allowed quantification of key characteristics of the flowfield, including circulation, vorticity, vortex trajectory, and induced rolling moments. Experiments were conducted for a variety of model angles of attack, tail incidence angles, and tail spans. The results showed that with high tail/wing circulation ratios (high tail downloads) the tail and wing vortices interacted strongly, leaving substantially weakened vortices after a distance of about 60 to 70 spans downstream of the model. A longitudinal static stability analysis identified the moderate-to-high static margins required to achieve such circulation ratios.

Nomenclature

b = span
b' = vortex span
C_L = lift coefficient, L/qS
C_M = pitching-moment coefficient, $M/qS\bar{c}$
C_{RM} = rolling-moment coefficient, RM/qSb
c = chord
$\bar{c}$ = mean aerodynamic chord
L = lift
N = number of wing spans
q = dynamic pressure, $\frac{1}{2}\rho V^2$
Re_c = chord Reynolds number, $V\bar{c}/\nu$
Re_Γ = circulation Reynolds number, Γ/ν
RM = rolling moment
S = wing reference area
t = time
u = freestream velocity
v = vortex descent speed
x = downstream distance
α = angle of attack
Γ = circulation
ν = kinematic viscosity
ρ = density
τ = nondimensional time, $t(v_0/b')$

Subscripts

F = follower aircraft
G = generator (lead) aircraft
T = tail
W = wing
0 = initial condition (immediately downstream of model)

Configuration Definitions (for example, [b3 w4 t1 g40 r207], or [b— w6 t— g— r190])

b# or b— = tail-to-wing span ratio, where # is expressed in tens of percent, or — means not defined because tail or wing is off
g# or g— = negative of estimated tail-to-wing circulation ratio, where # is expressed in percent, or — means not defined
r# = run number
t# or t— = tail geometric angle of attack (neglecting wing downwash), where # is expressed in degrees, or — means tail off
w# or w— = wing geometric angle of attack relative to freestream, where # is expressed in degrees, or — means wing off

Introduction

TRAILING wake vortices from an aircraft can present a serious hazard for following aircraft, especially in the terminal environment where the margins for recovery can be very slim. A satisfactory level of safety is currently achieved by requiring 2.5 to 6 nm of longitudinal separation between aircraft in trail (depending on the relative categories of the aircraft), which significantly limits the capacity of busy airports during peak hours. Even with these conservative separation standards, dangerous wake-vortex encounters still occur.

Many efforts to reduce this wake hazard have focused on either wake avoidance or alleviation by a wide variety of means. Avoidance refers to a method of detecting the location of hazardous vortices in the airport terminal environment and providing guidance to air crews to steer around them.[1–4] It would have good potential for allowing reduced spacing if such a system could be matured and confidence in it established, but the technique is still in the research stage and is not yet ready for implementation in today's air traffic environment.

Alleviation refers to modifying the configuration of the vortex-generating aircraft so that the shed wake is less hazardous to aircraft

---

Presented as Paper 2004-1073 at the 42nd Aerospace Sciences Meeting & Exhibit, Reno, NV, 5–8 January 2004; received 5 February 2004; revision received 6 August 2004; accepted for publication 12 August 2004. This material is declared a work of the U.S. Government and is not subject to copyright protection in the United States. Copies of this paper may be made for personal or internal use, on condition that the copier pay the $10.00 per-copy fee to the Copyright Clearance Center, Inc., 222 Rosewood Drive, Danvers, MA 01923; include the code 0021-8669/05 $10.00 in correspondence with the CCC.

[*] Aerospace Engineer, Experimental Aero-Physics Branch; Don.Durston@nasa.gov. Senior Member AIAA.

[†] Research Scientist, Experimental Aero-Physics Branch; Stephen.M.Walker@nasa.gov. Senior Member AIAA.

[‡] Research Scientist, Experimental Aero-Physics Branch; David.M.Driver@nasa.gov. Member AIAA.

[§] Research Scientist, Experimental Aero-Physics Branch; Stephen.C.Smith@nasa.gov. Associate Fellow AIAA.

[¶] Professor, Mechanical Engineering Department; savas@newton.berkeley.edu. Associate Fellow AIAA.

following within distances shorter than the current Federal Aviation Administration mandated minimums. A number of vortex alleviation devices—wing-tip modifications, air injection, wing-tip turbines, fins, unusual combinations of flap, spoiler, and aileron deflections, etc.—have been tried in various studies[5–7] to dissipate or break up the wake vortices. Some devices have been more successful than others in modifying the vortex flowfields, but so far none of them have proven to be effective without imposing significant weight, lift, or drag penalties on the aircraft.

An extensive amount of wake-alleviation flight testing[5,8] was conducted during the 1970s using heavy aircraft such as a Boeing 747 or a Lockheed L-1011. Some of the techniques seemed to work well, but, as an example of how elusive some of the solutions can be, it was surprising to find that lowering the landing gear nullified the wake-alleviating effects of certain configurations.

A promising technique now being investigated at Boeing involves oscillating the ailerons and spoilers to create large-scale instabilities that cause the vortices to pinch off into rings much sooner than they would under a typical Crow instability.[9] The oscillations are done in such a way that the overall lift is held relatively constant and there is no net rolling moment. A flight-simulator study of this technique has shown that the wake hazard is substantially reduced once the vortices pinch off into rings[10] and can lead to full-scale validation flight tests in the future.

The motivation for the current wake-alleviation study arose from research conducted at University of California Berkeley,[11–13] in which significant reductions in the vortex strengths were achieved by using a passive system involving outboard-mounted triangular flaps on a rectangular wing. The inboard edges of the flaps (formed by the midspan chord extension defining the triangle) generate vortices that are counter-rotating relative to the wing-tip vortices, and these, being weaker, wrap around the tip vortices and reduce their concentrated vorticity much faster than would happen without the flaps. Although the outboard-mounted flaps would entail excessive structural penalties for the wing as a result of the high outboard loading, it is the concept of the counter-rotating vortices that led to our thinking that a horizontal tail should be able to produce the same effect as the triangular flaps. The tail on a stable, conventional aircraft typically carries a download to counteract the wing's nose-down pitching moment, and thus generates vortices that are counter-rotating relative to the wing-tip vortices. The present study was therefore undertaken to investigate the tail geometries and downloads that would lead to accelerated destruction (or at least weakening) of the wing-tip vortices. Advanced instrumentation in the form of particle image velocimetry (PIV) combined with flow visualization (FV) was used to yield insights into the nature of the flowfield and the mechanisms for the vortex strength reduction.

Test Facility

The water tow tank used in this study, a facility of the University of California (UC) at Berkeley, is 60 m long, 2.4 m wide, and has a nominal water depth of 1.5 m. Observation windows, 1.1 m high with a total length of 3.3 m, are located at the center of the tank on one side. These permit viewing as well as illuminating both above and below the water surface. The glass windows are of sufficient optical quality so as to permit the transmission of laser light as well as viewing by high-resolution cameras.

The usable towing distance is typically 52 m, which has proved to be more than adequate for achieving stabilized conditions in the observation area. The model is accelerated to the desired speed and stabilized well before the test section and stopped far enough downstream so that the disturbances from stopping do not affect the wake behavior in the observation section within typical data-gathering time periods.

The approach of using a water tow tank was chosen for this study because of the advantages of towing the model through a quiescent medium: the freestream turbulence is very low, vortex meander is not an issue, and vortex motions can be observed for long periods after model passage.

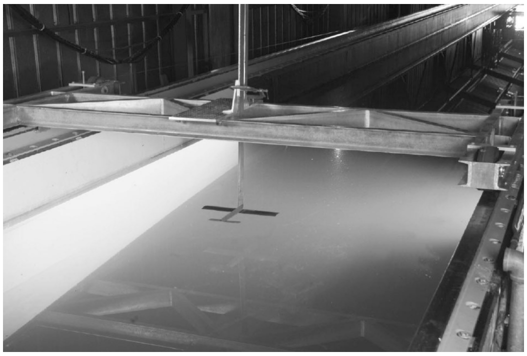

Fig. 1 View of tow tank test section looking downstream, with wing-tail model suspended from carriage.

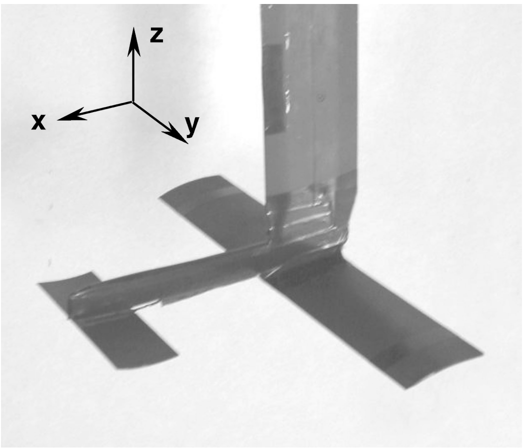

Fig. 2 Close-up of model suspended by strut.

Figure 1 shows a view of the tank with the model suspended from the carriage. The aluminum-frame carriage is towed along rails down the length of the tank by a steel cable driven by a 5-hp computer-controlled servomotor. The model was towed at a speed of 5 m/s through the water, giving a Reynolds number based on wing chord of 320,000. A dye delivery system was mounted on the carriage (not shown) to provide the fluorescent dye to the wing and tail tips. The water was illuminated with blue-filtered halogen lights on the right side of the tank for flow visualization.

Model Description and Test Techniques

Model

A generic, unswept wing-tail model (Fig. 2) was built with a fixed wing and a variable-incidence-angle horizontal tail, with two alternate tails of different spans available. The relative strengths of the wing and tail trailing vortices could be controlled by changing model angle of attack, tail incidence, or tail span. The model was designed to create a wake structure similar to that of the UC Berkeley triangular-flapped wing model, but with a more conventional wing-tail layout. As on the Berkeley model, the wing and tail were made from thin steel sheets (approximately 3.5% thickness-to-chord ratios) and were cambered about 5% to generate reasonably high lift coefficients at low-to-moderate angles of attack. The leading edges of the surfaces were rounded, and the trailing edges were tapered over the last 20% of the chord to thin edges. A brief wind-tunnel test was conducted at NASA Ames Research Center with this model to check for flow separation at the tow tank test conditions, and minimal separation was observed only at the highest angles of attack (above 10 deg) using surface oil flow visualization. No boundary-layer trips were used on the lifting surfaces in either the tow tank or the wind tunnel.

The three different horizontal tails have spans of 30, 40, and 50% of the wing span. The 30 and 40% span ratios were chosen to mimic those found on typical subsonic transport aircraft, and the 50% span ratio was chosen to allow observation of the changes in vortex interactions when the tail vortices were placed in closer proximity to the wing vortices.

Table 1 Wake-vortex model geometric characteristics[a]

Parameter	Wing	30% Tail	40% Tail	50% Tail
Span	41.91	12.70	16.76	20.96
Chord	6.96	5.08	5.08	5.08
Aspect ratio	6.02	2.50	3.30	4.13
Area	292.7	64.5	85.1	106.5
Tail arm[b]	——	18.26	18.26	18.26
Incidence, deg	4	−9–4	−9–4	−9–4

[a] All dimensions in cm or cm^2. [b] Tail arm is from wing $c/4$ to tail $c/4$.

The wing was fixed on the fuselage, but the incidence angle of the tail could be varied from −9 to +4 deg. Angle of attack of the model was set by selecting mounting holes on the carriage bracket (to which the strut attaches) that allow for variation in the strut pitch angle from −12 to +12 deg in 1-deg increments.

The geometric characteristics of the model are given in Table 1. The model was purposely sized small for the tank (42-cm wing span vs 240-cm tank width—17% ratio) so that the effects of the tank sides on the vortices would be minimal and to allow plenty of distance for the vortices to descend before being influenced by the bottom of the tank. The model was typically run at a depth of 40 cm, leaving 110 cm to the bottom of the tank. It was observed in the flow visualization that the dye became too diffuse to see long before the vortices came near to the bottom. Regarding the PIV images, the lower edge of the image area was about halfway between the model and the bottom of the tank, so that it is reasonably safe to say that any possible effects of the tank bottom on the vortices would not be observed in the PIV data.

Model sideslip angle was set as close as possible to zero by aligning the model with the strut and by lining up the strut with the axis of the tow tank. The strut was aligned for zero yaw by mounting a HeNe laser on it and adjusting the strut yaw to line up the laser beam with the tank centerline. A known, small twist in the strut between the model and the mounting end was compensated by yawing the strut at the mounting end by an amount equal and opposite to that of the twist.

The strut was made as thin as possible (0.8 cm thick) to try to minimize the interference of its wake with those of the wing and tail. The thinness of the strut was limited by the strength requirements to hold the model steady and secure and by the need to pass the four dye tubes through it. Selected dye flow visualization runs with dye exiting at the bottom of the strut without the model attached, or at the bottom of the model fuselage (0.8 cm thick by 2.54 cm high) with the wing and tail off, revealed the small, turbulent wake from the strut and fuselage.

Dye Flow Visualization

Fluorescent dye flow visualization was performed in order to observe and record the vortex motions and make qualitative judgments about the nature of the interactions. To accommodate the flow visualization, 1-mm (0.040-in.) dye tubes were routed from dye reservoirs on top of the carriage, through the strut and the fuselage, inside the leading and side edges of the wing and tail, and terminated along the side edges within 0.5 cm of the trailing edges. The dye used was a fluorescent yellow/green water-tracing dye (fluorescein), used mostly in 100-1 concentration. Dye flow was triggered on and off over a 1-s interval as the model passed the test section so that the amount of dye introduced into the tank for each run would be kept to a minimum to preserve water clarity.

An array of six carousel slide projectors and 18 halogen spot track lights, all with blue dichroic filters (transmitting light in wavelengths from 400 to 500 nm), illuminated the test section to make the dye visible to the cameras. Two Sony digital video cameras (TRV-20 and TRV-900) were used to record the dye flow runs. One was mounted inside a clear plastic tub partially submerged in the tow tank to provide a $\frac{3}{4}$ rear view of the model passing the test section. The tub was an open-top rectangular box in which the camera was placed with the lens slightly below the water line, and it was located to the right of center in the tank (to allow passage of the model strut) about 2 m upstream of the test section (i.e., towards the starting end of the tank). The other video camera was mounted outside the side window of the test section to give a nearly direct side view. Video recordings of the wake flowfield were made for as long as the dye remained concentrated and visible enough for the vortex interactions to be observed (typically 10 to 15 s).

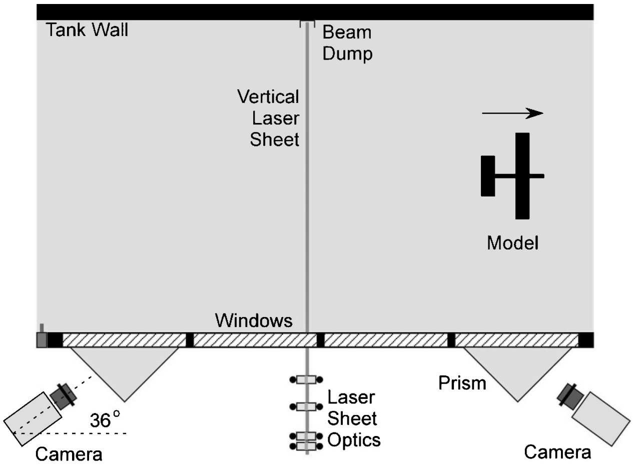

Fig. 3 PIV setup schematic; top view.

Particle Image Velocimetry

Three-dimensional PIV was used to measure fluid velocities in a vertical plane perpendicular to the axis of motion of the model. A schematic of the PIV system is shown in Fig. 3. This system used off-axis stereoscopic viewing, based on a two-axis Scheimpflug camera system, for perspective viewing of the three-dimensional wake behind the model. To eliminate refraction from viewing obliquely through the air-glass-water interface, a water-filled prism was mounted and sealed to each window in front of the cameras.

A dual-head, Spectra Physics PIV-400 Nd:Yag laser emitting at 532 nm was used as the light source. The laser puts out a pair of 350-mJ pulses for each PIV image pair, where instantaneous velocities are calculated from the particle displacements between the two images. The duration of each pulse is 16 ns with a time delay of 535 μs between pulses. The laser sheet was created using four cylindrical lenses, and seeding was provided by 40-μm-diam silver-coated hollow glass spherical particles. These particles were manufactured by Potters Industries, Inc., and had a specific gravity of 0.9.

The two cameras were Kodak Megaplus ES 4.0 (2048 × 2048 pixels), and the camera frame rate was limited during testing to 2.5 Hz. For a model speed of 5 m/s, this corresponds to 2 m of model translation between successive PIV image pairs. The imaging lenses had a focal length of 35 mm and f# of 1.4. The camera system provided an area of image capture of approximately 1.0 m high × 1.3 m wide. ProVision software[14] was used for data acquisition, which was triggered by model passage.

A photograph of the PIV installation is shown in Fig. 4. The vertical light sheet spanning the tow tank can be seen in the figure, though it appears to be narrower in height than it really is because of the distortion in looking obliquely through the water surface. The different lighting requirements between the PIV and the FV runs precluded the simultaneous acquisition of both types of data. The usual test procedure was to make a number of FV runs and then acquire PIV images for a subset of these runs. This process was repeated a number of times throughout the duration of the test program.

Experimental Data and Analysis

In preparation for selecting the model configurations to run (angle of attack, tail span, and tail incidence angle), a review was made of the span and circulation ratios noted in the literature that have led to the mutual vortex interaction and breakdown. Some studies[15–18] have indicated that such destructive interactions occurred when the

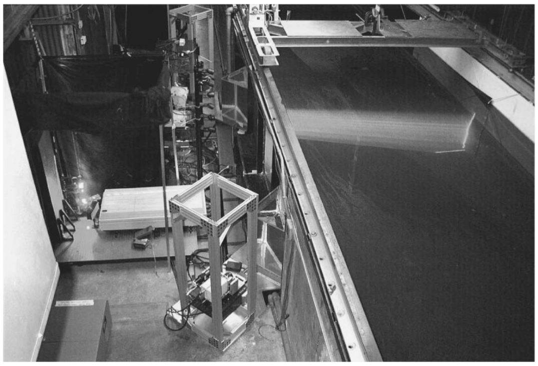

Fig. 4 PIV setup at tow tank test section.

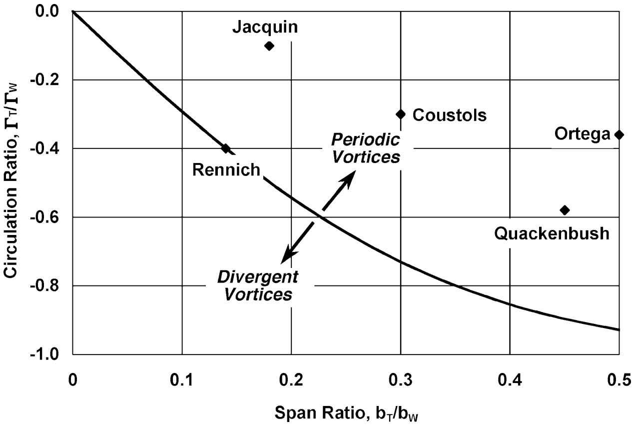

Fig. 5 Criterion for destructive vortex interaction.

circulation ratio between the wing-tip vortices and those from other surfaces (flaps, horizontal tail, and/or various fins or other vortex-generating devices) was in the range of roughly −15 to −75% for span ratios ranging up to 0.5. Figure 5 (compiled from Refs. 14 and 15) shows a graphical representation of this criterion for destructive interaction, with test points from the work of several researchers indicated. The point marked "Ortega" is from the studies of the triangular-flapped wing[11–13] that led to the present study. The curved line separating the "divergent" from the "periodic" areas represents an approximate upper limit of the circulation ratios (in an absolute value sense) that lead to accelerated vortex destruction. It is defined by the following equation from Ref. 15:

$$\frac{\Gamma_T}{\Gamma_w} = -f\,\frac{\left[3(b_T/b_W) + (b_T/b_W)^3\right]}{\left[1 + 3(b_T/b_W)^2\right]} \tag{1}$$

where f is a factor that can be used to define a transitional area if desired, but has the value of one in this case.

In Fig. 6, the criterion plot is repeated in order to show which configurations were tested in the present study, which ones will be highlighted in this paper, and the approximate ranges of typical span and circulation ratios for aircraft currently flying. It is entirely possible that those aircraft with the higher span and circulation ratios are already achieving some level of accelerated vortex destruction, which could be revealed through flight-test measurements.

To identify the wing-tail model configurations that would achieve this vortex destruction, estimates of the lift of each configuration were made with the LinAir[19] vortex lattice aerodynamic prediction code. This code, being inviscid and based on lifting-line theory, tends to overpredict the lift at moderate to high angles of attack because of the lack of boundary layer and separation effects. Because all of the runs in the present test were conducted with wing angles of attack of 10 deg or less (where no significant separation was observed in wind-tunnel tests), it is believed that the LinAir lift estimates used in this study are within a few percent of the correct values, and thus the errors should have no significant effect on the overall results presented herein.

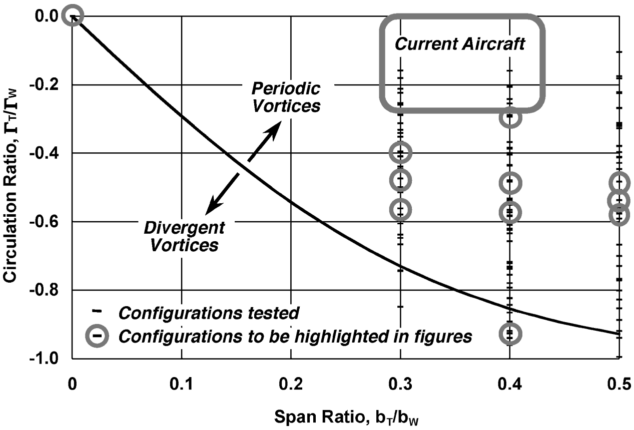

Fig. 6 Present test configurations.

The ratios of the estimated lift divided by the span for the wing and tail were used to predict the relative vortex strengths between the wing and tail, as in the following equation:

$$\frac{\Gamma_T}{\Gamma_W} = \frac{L_T/b_T}{L_W/b_W} \tag{2}$$

Configurations that yielded vortex-strength ratios in this range, and somewhat beyond both ends of this range, were therefore selected for testing. A total of 192 dye flow runs and 137 PIV runs were done in the tow tank, though many of the early runs were not useful because the test setup and technique were still being refined.

The discussion will begin with some of the dye flow visualization runs in order to illustrate representative vortex flow patterns. Then, PIV data will be introduced to supplement the dye flow results.

Flow-Visualization Runs

FV runs showing the behavior of a single pair of vortices are presented first in order to show the persistence of an undisturbed pair of vortices with this model. A wing-alone configuration (including fuselage) at 8-deg angle of attack is shown in Fig. 7. The model was painted black for the PIV runs, and thus does not show up well in the videos, and so the image of the model in the first frame a) is outlined in white for clarity. The time scale τ noted for each FV frame is a nondimensional time parameter defined as

$$\tau = t(v_0/b') \tag{3}$$

where

$$\nu_0 = \Gamma_0/2\pi b' \tag{4}$$

with t being real time, v_0 being the initial vortex descent speed, b' being the initial wing-tip vortex spacing (as measured by PIV), and Γ_0 being the initial total circulation of the wing-tail vortex system (as predicted by LinAir). The LinAir-predicted lift coefficient is given in the figure caption for reference.

The model is just passing the test section in the first frame (traveling from left to right, as is true for all dye flow images presented herein). The dye can be seen flowing smoothly from the wing tips, but some dye is also leaking from the bottom of the fuselage. This dye is coming from the tail dye tubes, which are terminated in the fuselage, but they were not perfectly sealed. Fortuitously, this dye identifies the small, turbulent wake of the fuselage.

The following frames (b–d) show the wing-tip vortices remaining intact and stable as they descend in the test section. Note that in frame d), the vortices (at the bottom of the image) are very faint, both because of dispersion of the dye and their moving out of the light, but still show no signs of instability or interaction. This remained true as observed by eye in real time for longer than the length of the video recorded (over 12 s).

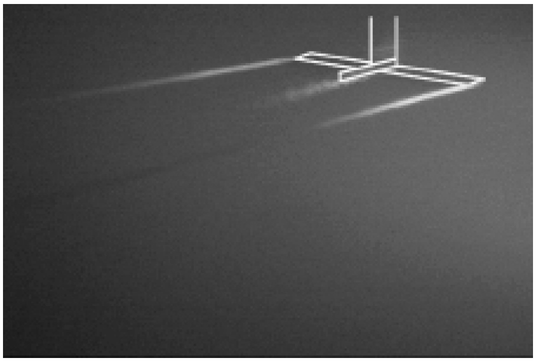

a) At model passage, $\tau = 0$

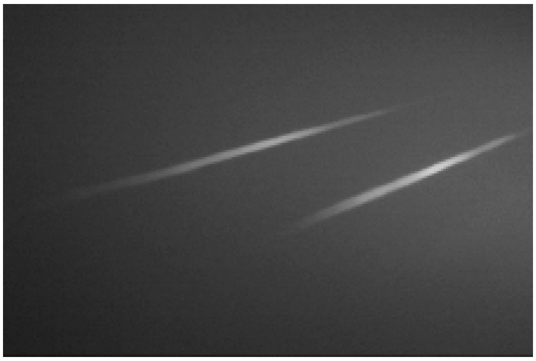

b) $\tau = 0.65$

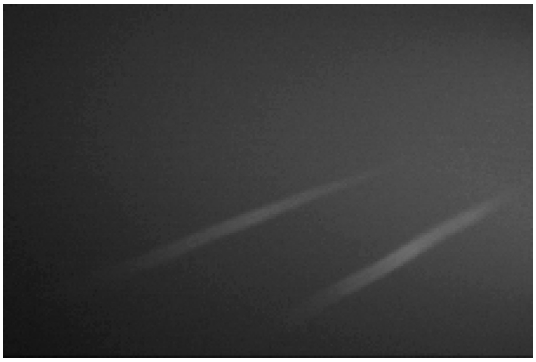

c) $\tau = 1.29$

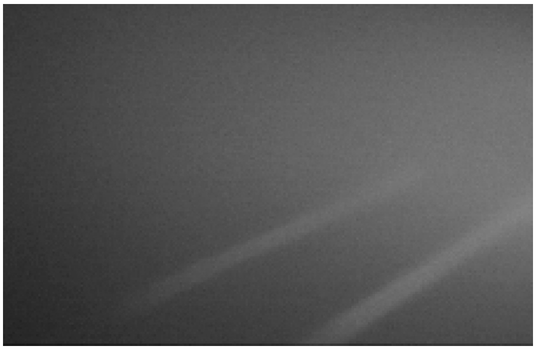

d) $\tau = 1.72$

Fig. 7 Wing-alone configuration [b— w8 t— g— r135]; $C_L = 0.980$.

FV runs for the wing-tail configuration showed dramatic interaction between the wing and tail vortices (Fig. 8). The two runs in the figure, 195 showing a rear view on the left and 190 showing a side view on the right, are of the same configuration and test conditions, [b4 w6 t0 g48]. Run 195 was a repeat of 190 and is shown here because its quality is better than the rear-view video for Run 190, and the side-view video for 190 is of better quality than for 195.

The frames from the two runs were matched up as best as possible by comparing the development of the loops in the tail vortices and the time at which the tail vortex first contacted the wing vortex. The result of this matching yielded frames that appear to be fairly well synchronized visually, but the times of the frames do not agree very well, as seen in the subfigure captions. Considering Fig. 8e, the tail vortex first contacts the wing vortex at $\tau = 0.383$ (about 3 s in real time) after model passage in run 195, but at $\tau = 0.508$ (about 4 s) in run 190. The reason for this difference is probably because the vortex instabilities are excited by random background forcing and thus cannot be expected to guarantee comparable repeat runs of the same configuration. Such differences in timing among various repeat runs were not atypical throughout the FV and PIV testing, and they give an indication of the uncertainty in the time measurement in the FV runs. A review of a number of sets of repeat runs revealed that the average difference in the timing of this first contract between vortices was on the order of 0.5 s within the first 4 to 5 s of data.

Determining the time at which the tail vortices first contacted the wing vortices is a very subjective process when the dye is faint. Variables among the runs such as concentration of the dye in the vortices, vortex stability, water clarity, and residual turbulence all affected the quality of the images obtained in the videos and thus the ability to gather useful quantitative as well as qualitative information from them. Run 190 had the most clearly defined vortices and was the best video out of all of the runs taken in these tests, and so it was fairly easy to observe the vortex motions for this run, but it was not as easy for some other runs.

In regards to the vortex behavior in Fig. 8, the tail vortices, having a predicted 48% of the circulation of the wing vortices (and opposite in rotation), are seen to orbit around the wing vortices because of the latter's stronger influence. The tail vortices fairly quickly form into Ω loops (owing to their shape), which get drawn over the tops of the wing vortices. Once the tip of a tail vortex loop starts to wrap around the wing vortex, it makes contact with it, and part of the tail vortex appears to merge with the wing vortex while other parts appear to break off and move upward away from the wing vortex (as can be observed in frames f), g), and h) of Fig. 8). What happens after this is not clear from the FV images because the dye becomes too diffused to be seen. This lack of information leaves open the possibility that the end result is a just pair of weakened wing-tip vortices, but there are still the remnants of the tail vortices above them. One possibility of what happens to these remnants is what Ortega and Savaş[11] describe in their tests of the triangular-flapped wing: the remnants form loops after breaking off from the wing vortices, then they pinch off, forming vortex rings, and cross the centerline. Whether or not this mixing across centerline affects the weakened wing-tip vortices is not discernable either in the videos of the present study or in Ortega's videos.

The foregoing was an example of vortex interactions for a case with moderately strong tail vortices. Other cases for weaker and stronger tail vortices will now be shown to illustrate the extremes of the tail/wing vortex interactions.

A case with relatively weak tail vortices is configuration [b4 w8 t3 g29 r133], for which the tail/wing circulation ratio is now -0.29. This ratio is probably closer to that of typical transport aircraft (though still a bit high), hence a little more representative of realistic wakes than those for the preceding runs. Two pairs of images from the videos of run 133 are shown in Fig. 9; the first rear- and side-view pair showing the vortices at $\tau = 0.148$ (within $\sim$10 spans of model passage) and the other pair at $\tau = 0.604$ (about 30 spans later) as the tail vortices are interacting with the wing vortices.

There are two striking differences between these images and those of runs 190/195: 1) the tail dye flow is much weaker and more diffuse, and 2) the wing vortices are much less affected by the tail vortices. The reasons for both of these differences are the same: with the tail at a geometric angle of attack of +3 deg and its circulation less than $\frac{1}{3}$ of that of the wing, the tail vortices are much weaker than in Fig. 8. Thus their influence on the wing vortices is much less, and there is very little wake alleviation with this configuration. It is apparent that in Fig. 9b the wing-tip vortices are still fairly

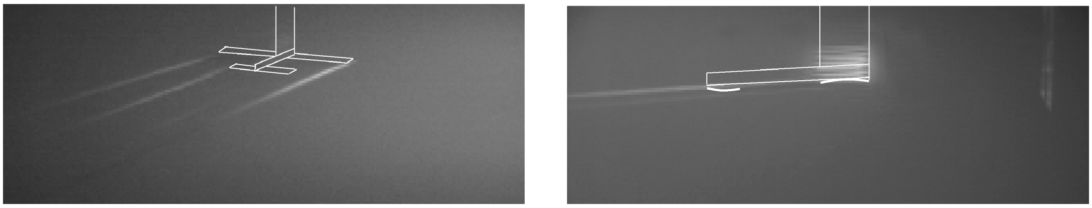

a) Rear view: at model passage; τ = 0 **a) Side view; τ = 0**

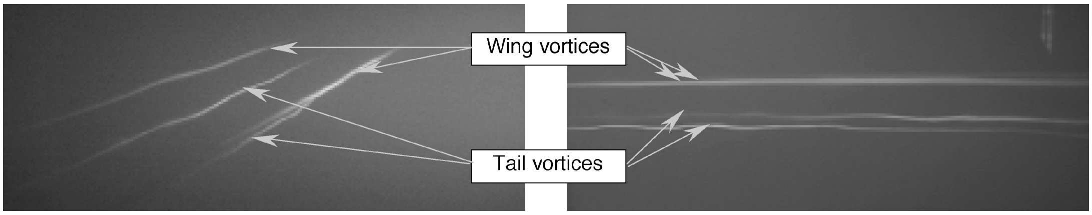

b) τ = 0.112 **b) τ = 0.151**

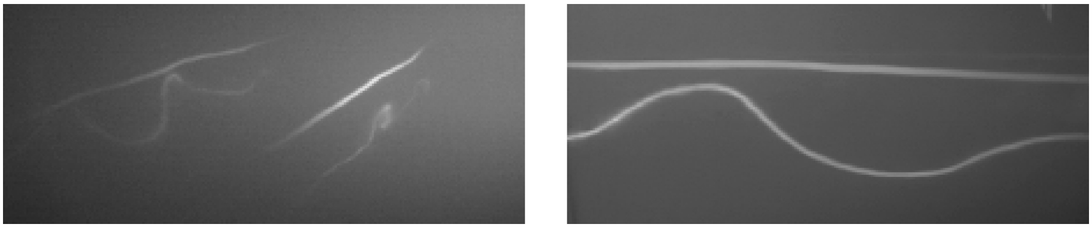

c) τ = 0.310 **c) τ = 0.413**

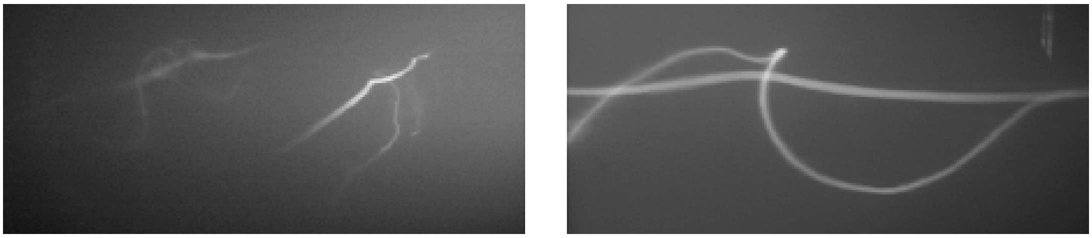

d) τ = 0.379 **d) τ = 0.500**

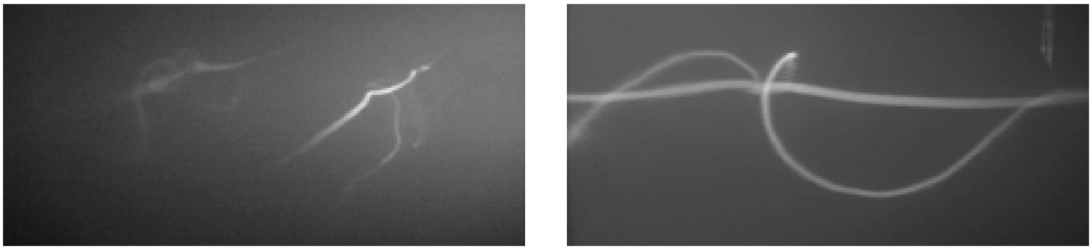

e) τ = 0.383 **e) τ = 0.508**

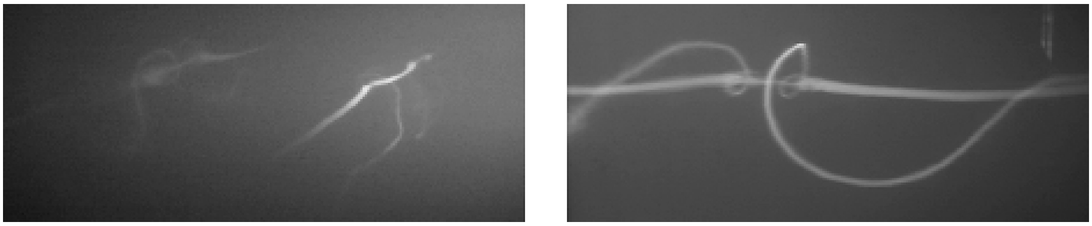

f) τ = 0.392 **f) τ = 0.517**

Fig. 8 Wing-tail (40% span) configurations ([b4 w6 t0 g48 r195] rear views: left and [b4 w6 t0 g48 r190] side views: right); C_L = 0.671.

coherent, though spreading (or at least the dye is spreading) under the influence of the tail vortices.

A case with very strong tail vortices is configuration [b4 w3 t-5 g92 r241], shown in Fig. 10. The tail vortices are strong enough (having 92% of the wing vortex strength) in this case so that they diverge upward from the wing vortices, just as an isolated pair of vortices would from a downwardly loaded lifting surface. In the first pair of images ($\tau = 0.133$), the tail vortices have moved significantly above the wing vortices and are starting to develop their own instabilities. In the second pair ($\tau = 0.196$), the tail vortices have moved upward a little further and are starting to break apart without much apparent influence on the wing vortices. This clearly is not a wake-alleviation configuration and demonstrates the expected vortex behavior when the tail download is too high. This configuration is the test point circled in Fig. 6 just below the periodic/divergent boundary curve and is consistent with the assertion

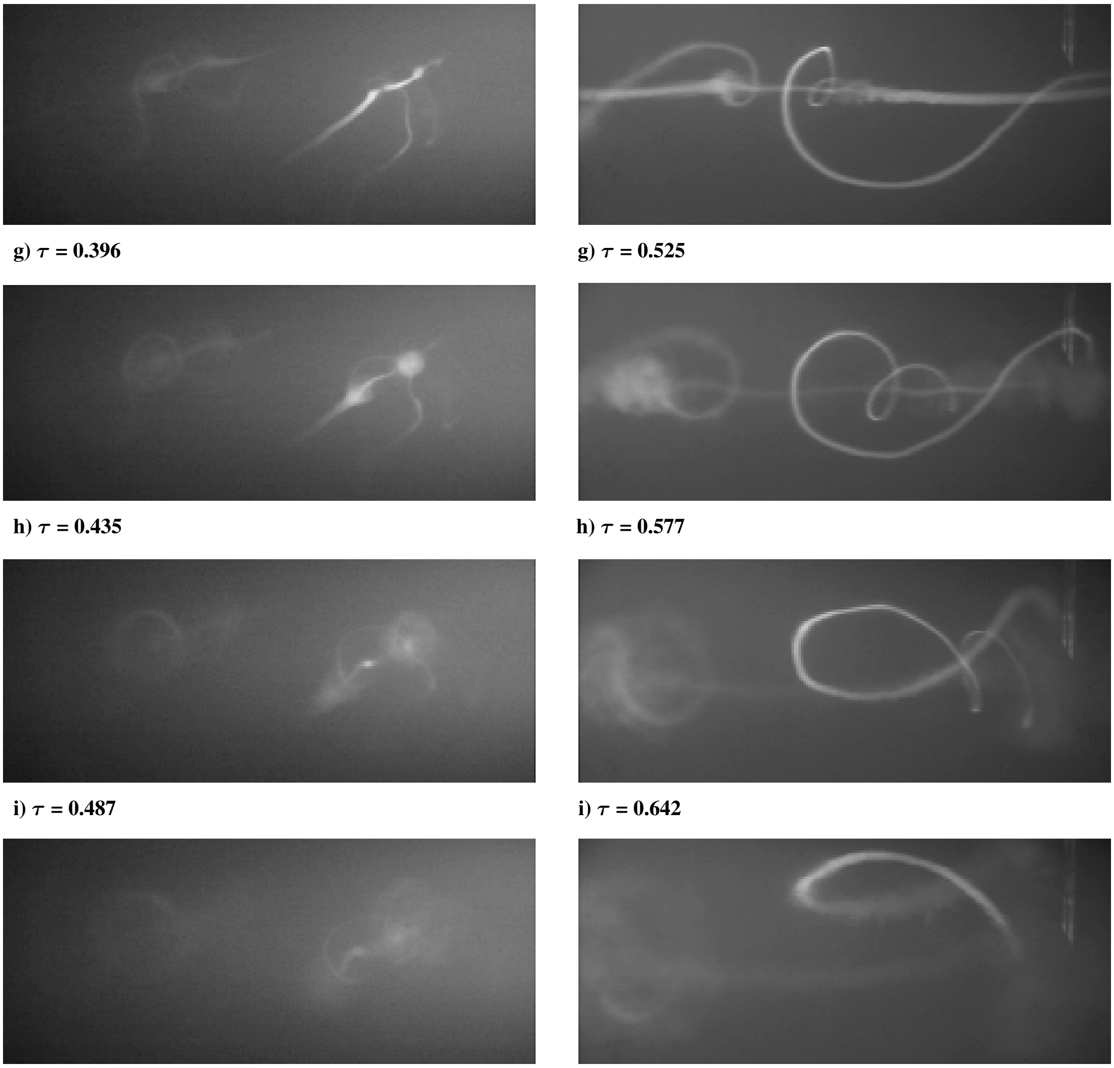

g) τ = 0.396 **g) τ = 0.525**

h) τ = 0.435 **h) τ = 0.577**

i) τ = 0.487 **i) τ = 0.642**

j) τ = 0.543 **j) τ = 0.719**

Fig. 8 Wing-tail (40% span) configurations ([b4 w6 t0 g48 r195] rear views: left and [b4 w6 t0 g48 r190] side views: right); C_L = 0.671 (continued).

that configurations below the boundary will have divergent pairs of vortices.

Dye flow visualization results for the other two tails used with this model, having 30% and 50% of the wing span, are shown in Figs. 11 and 12, respectively. These figures show that a similar mechanism for the vortex interaction occurs for these configurations as for the 40%-span ratio configuration.

The first pair of images for the 30%-span tail in Fig. 11 shows the tail vortices descending below the wing vortices as for the 40%-span tail, but in this case there are more short-wavelength instabilities, and the dye is more diffuse at this point ($\tau = 0.253$). By the second pair of images for this figure ($\tau = 0.777$), the tail vortices have already looped around the wing vortices, and the resulting spirals are apparent in the side view.

Figure 12 shows similar characteristics for the 50%-span tail, but in the latter pair of images ($\tau = 0.355$) the dye in the tail vortices is already very diffuse, almost to the point of not being able to recognize the formation of the Ω loops around the wing vortices. The loops are quite apparent in the video, however, and can be seen faintly in background of the $\frac{3}{4}$ rear-view image at $\tau = 0.355$.

PIV Runs

Three-dimensional planar PIV allows the determination of a number of parameters useful in characterizing the flowfield. In this section, selected results are shown to quantify the effectiveness of certain configurations in achieving accelerated vortex destruction.

Vorticity Contours

Contour plots of the x component of vorticity (axial) are shown in Fig. 13 for the wing-alone and two wing-tail configurations. The configurations are compared at constant downstream distances in terms of span because the frame rate was not high enough to acquire enough frames to make comparisons at constant τ. The values of τ associated with each frame are indicated for reference and are determined from the distances in spans N by noting that $N = ut/b$. When combined with Eq. (3), the relation is

$$\tau = N(v_0/u)(b/b') \tag{5}$$

The vorticity contours for the wing-alone configuration (left column, [b— w8 t— g— r251]) show that the wing-tip vortices remain strong and coherent out to (and beyond) 124 spans downstream. There is very little change in the contour levels among all of the frames.

In contrast, the wing-tail configuration with a -0.29 circulation ratio (middle column, [b4 w8 t3 g29 r252]) shows a moderate diminishing of the vortex strengths with downstream distance. The wing-tip vortices in the first frame appear similar to those from the wing alone, but the vorticity is noticeably reduced by the last frame at 124 spans downstream. The tail vortices for this configuration are barely visible in the first frame but almost completely disappear by the second frame (ref. Fig. 9). The rate of descent of the wing-tip vortices is slowed by about half because of the influence of the tail vortices.

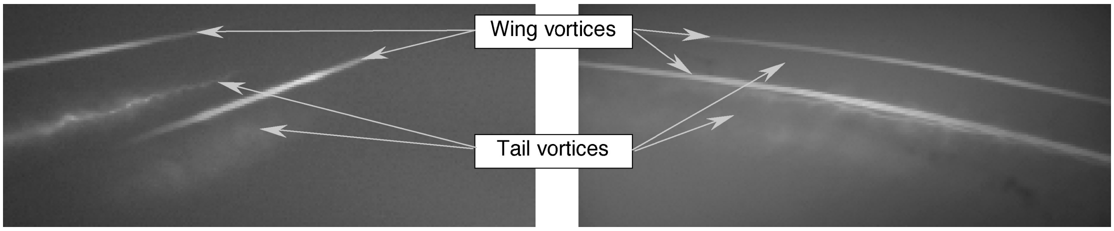

a) τ **= 0.148**

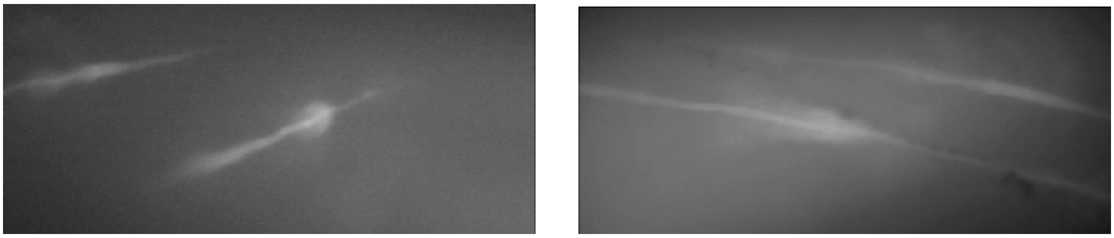

b) τ **= 0.604**

Fig. 9 Low circulation ratio wing-tail (40% span) configuration [b4 w8 t3 g29 r133] (rear views: left; side views: right); $C_L = 0.864$**.**

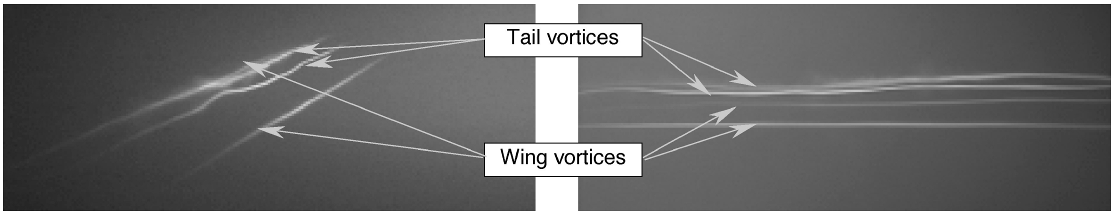

a) τ **= 0.133**

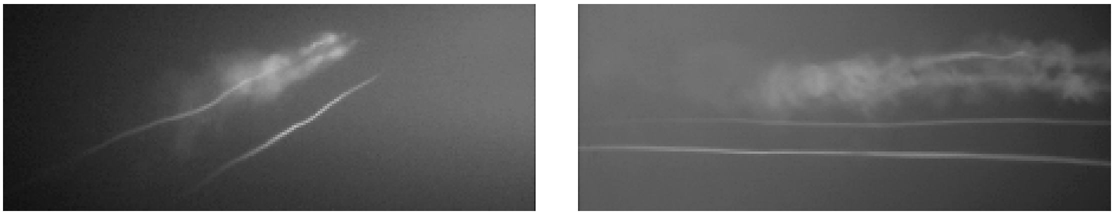

b) τ **= 0.196**

Fig. 10 High circulation ratio wing-tail (40% span) configuration [b4 w3 t-5 g92 r241] (rear views: left; side views: right); $C_L = 0.390$**.**

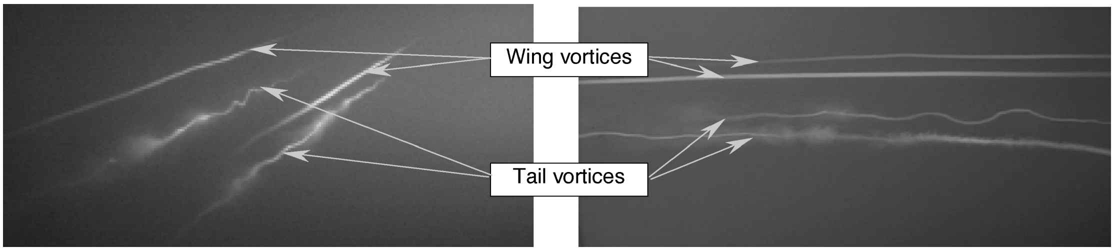

a) τ **= 0.253**

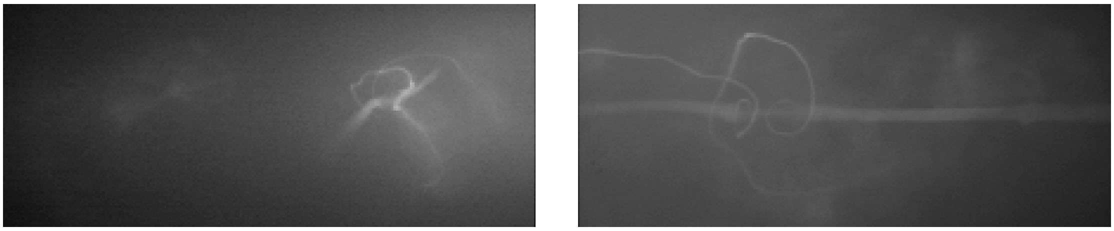

b) τ **= 0.777**

Fig. 11 30%-span ratio wing-tail configuration [b3 w4 t1 g40 r207] (rear views: left; side views: right); $C_L = 0.615$**.**

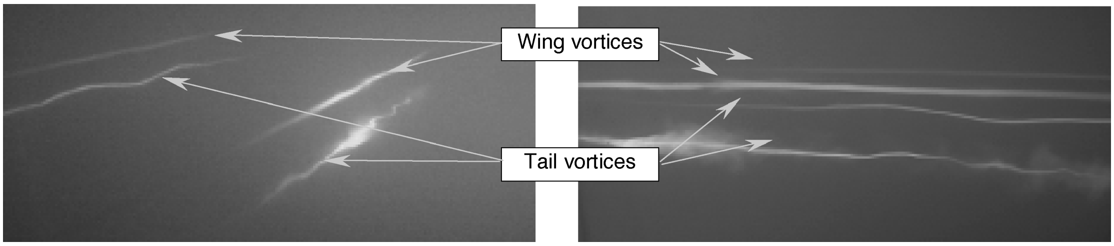

a) $\tau = 0.202$

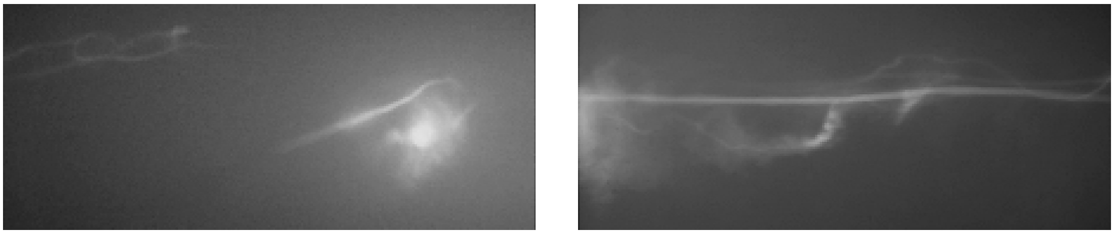

b) $\tau = 0.355$

Fig. 12 50%-span ratio wing-tail configuration [b5 w6 t0 g54 r176] (rear views: left; side views: right); $C_L = 0.606$.

As the tail/wing circulation ratio increases to −0.48 (right column, [b4 w8 t-1 g48 r257]), the influence of the tail vortices on the wing vortices is much greater. The relatively strong tail vortices remain partially visible through the third frame (33 spans downstream), and the rate of descent of the wing vortices is slowed even further relative to the other two runs. By 124 spans downstream, the vorticity contours of the wing vortices are much smaller in size than in the other two runs.

The frames in Fig. 13 for all three configurations are shown at constant distances downstream. Because the vortices for the wing-alone case descend faster than for the other cases, there remain additional frames for the latter in which the vortices have not yet descended below the field of view or reached the data-acquisition frame limit. The last data frames acquired for the two wing-tail configurations are shown in Fig. 14, along with the last wing-alone frame at 124 spans downstream. (The vorticity scale is the same as in the preceding figure.) As indicated in the figure, the wing-tail configurations with the −0.29 and −0.48 circulation ratios are shown at distances of 229 and 276 spans downstream, respectively. It is immediately apparent that the vorticity magnitudes have dropped off considerably from the frames shown at 124 spans downstream in the preceding figure. The reductions in vorticity indicate that further diffusion of the already weakened wing vortices has taken place over the extended distances shown.

What the vorticity contours do not show are the remnants of the tail vortices after the merging process, as discussed in regards to the FV images in Fig. 8. These remnants could be above the upper boundary of the PIV image area, or be sufficiently nonnormal to the viewing plane or be weak enough that their vorticity is not captured above the background vorticity in the image. In any case, the last-frame PIV images do not reveal any information about possible further vortex interactions beyond that observed in the FV images, except for the noted reductions in vorticity. Thus, the current PIV data do not seem to shed any additional light on the far-field effects of the vortex instabilities. Hopefully, refinements in the FV and PIV test techniques in the future can yield more information in this flow regime.

Vortex Tracking

Tracking the centroids of vorticity in successive PIV frames shows the movement of the vortices under their mutual influences. Figure 15 shows this tracking for the three runs of Fig. 13. The numbers beside selected points along the vortex tracks show the downstream distance in spans; the τ values are shown only for the last points for each configuration but can be scaled linearly with the distances shown.

The airplane symbol (shown with tail off in the first subfigure) depicts the approximate wing and tail spans relative to the vortices. The wing-alone run in Fig. 15a shows the vortices rapidly descending and going below the field of view shortly after 100 spans. The fact that the vortex descent paths are fairly straight and do not diverge as they reach the bottom of the PIV field of view indicates that there does not seem to be any appreciable influence of the tow tank floor on the vortices. The tank floor is 110 cm below the model, well below the end of the vortex traces (at 65 cm).

In Fig. 15b, the relatively weak tail vortices appear only as single dots because their vorticity in succeeding frames fell below the cutoff (noise) value for plotting, caused part by the low spatial resolution of the PIV data. From the dye flow runs of this and similar configurations, the tail vortices were observed to move outward below the wing vortices and the rather diffuse dye appeared to be entrained into the wing vortex flowfield. Note also in Fig. 15b that the descent rate of the wing vortices has slowed considerably because of the influence of the tail vortices. The higher-strength tail vortices in Fig. 15c have enough vorticity to be tracked for more frames than in Fig. 15b, but again, their vorticity falls below the cutoff before wrapping around the wing vortices. Their stronger influence on the wing vortices is apparent, however, in the outward looping path taken by the latter before the “merged” vortex system starts descending.

This motion of the tail vortices going around the wing vortices below and to the outside demonstrates that the vorticity centroid for the vortex pair (on one side) is outboard of the vorticity centroid for a single vortex. This outboard shift causes the wake to effectively have a larger span, which has the effect of spreading out the circulation and thus reducing the hazard to smaller following aircraft—though this benefit might be lessened for large following aircraft. An adverse effect is that the wake descent rate is slowed, prolonging the period for which the wake remains in or near the flight path of following aircraft.

Rolling Moment

Rolling-moment induced on a following wing was chosen as the key parameter[6] for the determination of the hazard posed by a vortex wake. The moments were calculated by mapping a straight pseudowing, having 25% of the span of the model, in the grid of PIV-measured velocities. The measured velocities were applied to the pseudowing using strip theory to estimate the induced rolling moments. (No three-dimensional flow effects were considered on the following wing.) The maximum rolling moment over an entire PIV survey plane was found by calculating the moments at every survey point, and then the location and magnitude of the highest absolute

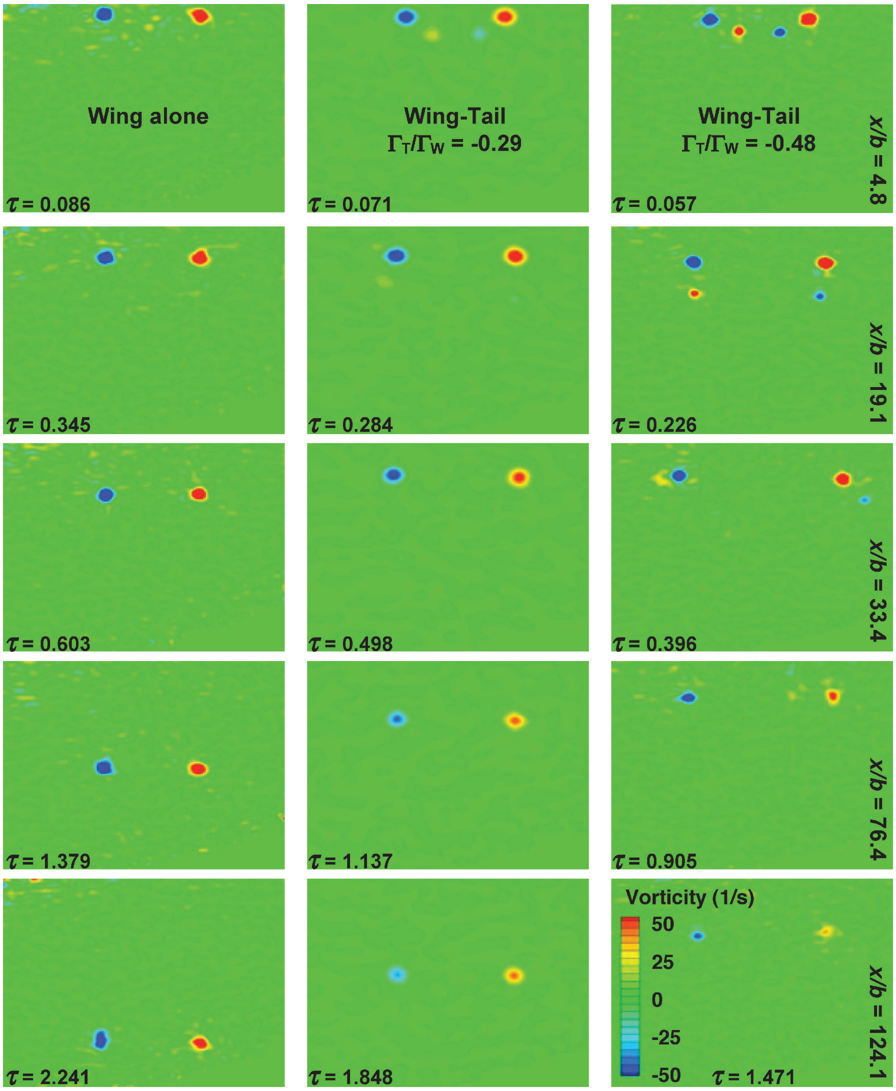

Fig. 13 Vorticity contours for wing-alone [b— w8 t— g— r251], left, and wing-tail (40% span) configurations [b4 w8 t3 g29 r252], center, and [b4 w8 t-1 g48 r257], right.


Wing-alone
τ = 2.241
x/b = 124.1

Wing-tail, Γ_T/Γ_W = -0.29
τ = 3.411
x/b = 229.1

Wing-tail, Γ_T/Γ_W = -0.48
τ = 3.281
x/b = 276.8

Fig. 14 Last-frame vorticity contours for wing-alone [b— w8 t— g— r251], left, and wing-tail (40% span) configurations [b4 w8 t3 g29 r252], center, and [b4 w8 t-1 g48 r257], right.

value of the rolling moment were recorded. This process was repeated for all survey planes in a given run in order to generate plots of the rolling-moment variation with time.

The moments (in coefficient form) are all normalized by the lift coefficient of the generating aircraft. This was done to enable comparisons of configurations with different circulation ratios based on a constant net lift of the generating aircraft. Higher circulation ratios are achieved in the present study with higher tail downloads, which in turn reduces the overall lift and thus represents a "penalty" for achieving wake alleviation. Normalizing all of the rolling-moment curves by the lift of the generator removes any apparent bias toward high-circulation-ratio configurations because of the adverse effect of the high tail downloads on the generator.

Rolling-moment variations with time are presented in the following figures as a way of summarizing the results from the many different runs of the model with the different span tails and with tail off. The first plot, in Fig. 16, shows the rolling moments for the three runs of Figs. 13 and 14 plus another run with a higher tail/wing circulation ratio. Note that the wing-alone curve is identified as such; the other three are identified as wing-tail configurations by virtue of

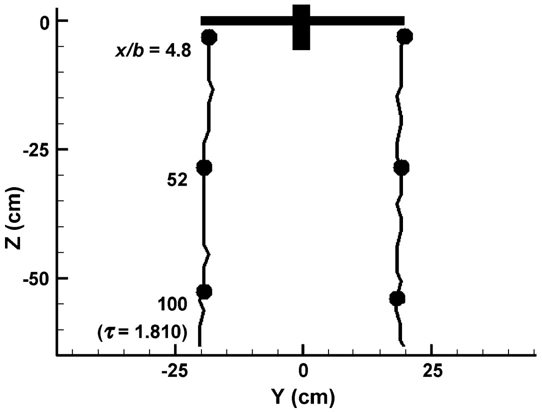

a) Wing-alone configuration [b— w8 t— g— r251]

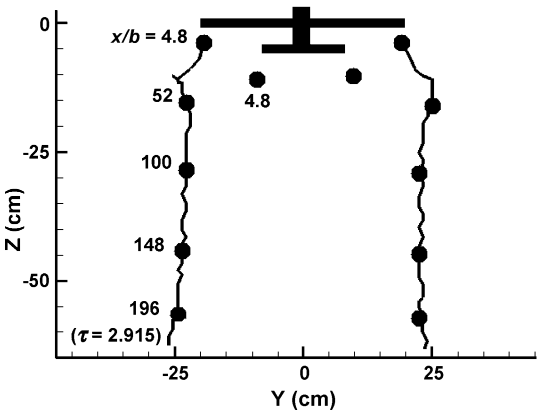

b) Wing-tail configuration [b4 w8 t3 g29 r252]

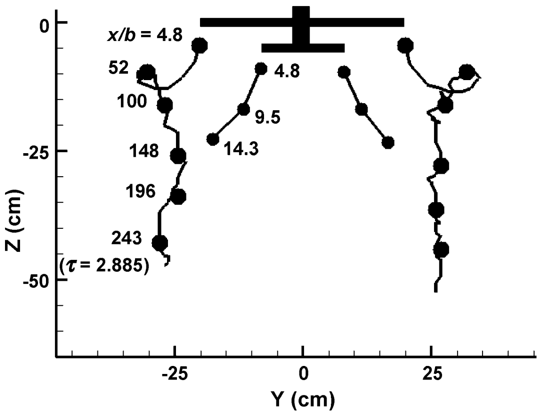

c) Wing-tail configuration [b4 w8 t-1 g48 r257]

Fig. 15 Tracking of vorticity centroids, $\alpha_w = 8$ deg.

Table 2 Representative airplane characteristics

	Aircraft type	
	Heavy	Large
Weight, lb	630,000	146,000
Wing area, ft^2	5,600	1,340
Vortex span b', ft	165	75
Approach speed, u, ft/s	270	270
Circulation Γ_0, ft^2/s	6,000	3,000
Vortex descent speed v_0, ft/s	5.7	6.4

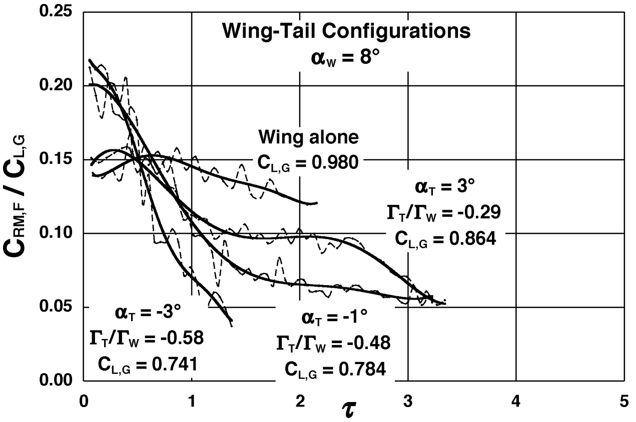

Fig. 16 Following-wing rolling-moment decay with time, wing-alone, and 40%-span tail configurations; $\alpha_W = 8$ deg.

the tail angle of attack (geometric angle, not including wing downwash effects) and the circulation ratios being specified. The dashed lines track the maximum moments in each survey plane, giving an indication of the typical scatter in the PIV data, and the solid lines are curve fits of these data.

The wing-alone configuration shows a gradual reduction in rolling moment after the initial peak, and the curve ends at about $\tau = 2$ because the rapidly descending vortices moved below the field of view of the laser light sheet. The curve with the -0.29 tail/wing circulation ratio drops well below the wing-alone curve, as the interaction of the tail vortices with those from the wing has weakened the latter, and thus the induced rolling moments are lower. This curve also extends further out in time because of the slower descent rate of the vortices after the interaction. The other curves with the higher circulation ratios drop even further, as expected based on the data observed in the preceding two figures.

The next two plots, in Fig. 17, show the rolling moments for all three tail-span configurations at wing angles of attack of 6 and 8 deg. Two primary observations can be made about these plots: 1) there is a general trend of more rapid rolling-moment decay with distance as the tail span increases, and 2) the rolling moments are typically lower for the configurations with the higher circulation ratios. Thus, as the tail is more highly loaded (downwardly) and its span increased, its vortices become more effective in accelerating the strength reduction of the wing tip vortices. Judging from the rapid drop-off in rolling moment to values of half or less than half of the initial values, one could surmise that the redistributing of circulation from the interaction of the wing and tail vortices generally (aside from some differences caused by tail span) results in the wing vortices having their strength reduced by the approximate magnitude of the tail vortex strength. A helpful illustration and discussion of this mechanism is presented by Ortega et al.[13] from their studies of the triangular-flapped wing, which created wakes and vortex structures very similar to those of the subject wing-tail configurations.

One might conclude from these rolling-moment trends, therefore, that more is better: even higher circulation ratios would lead to more rolling-moment reduction. However, at high tail vortex strengths (relative to the wing vortices) the influence of one tail vortex on the other is greater than the influence of the wing vortices, causing the tail vortices to travel upwards and away from the wing vortices. This was observed for circulation ratios above (in an absolute sense) approximately -0.75 to -0.90 (depending on span ratio), where the tail vortices had very little influence on the wing vortices (Fig. 10).

To give a real-world sense to these rolling-moment curves, the time data of Fig. 16 were scaled to full-scale aircraft by converting the time parameter τ to distance in nautical miles. Two sizes of aircraft were selected for presentation: a heavy aircraft, similar to a Boeing 747 in size, and a large aircraft, similar to a Boeing 737 in size. The magnitudes of the rolling moments were not changed, as the intent is to show the distances over which the wake hazard would persist for the generating aircraft having the same wake-alleviating configuration as the subject tow tank model but having the wake circulations, vortex spans, and approach speeds of the aircraft represented. The following equation, derived from Eq. (3), and the parameters in Table 2 (some of which were obtained from Ref. 10) were used to convert the timescales to distance:

$$x = ut = \tau b'(u/v_0) \tag{6}$$

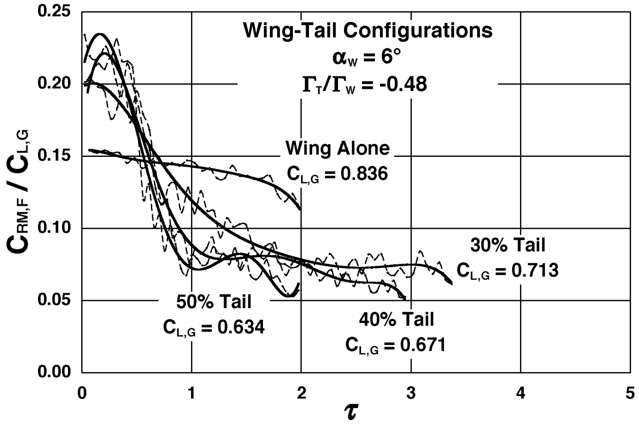

a) $\alpha_W = 6$ deg

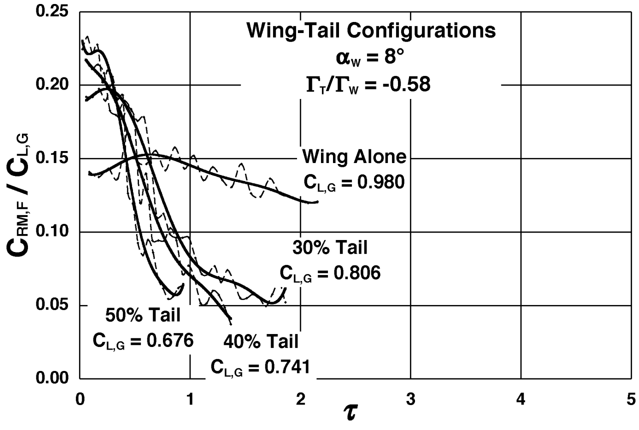

b) $\alpha_W = 8$ deg

Fig. 17 Following-wing rolling moment for wing-alone and three tail sizes on generating wing.

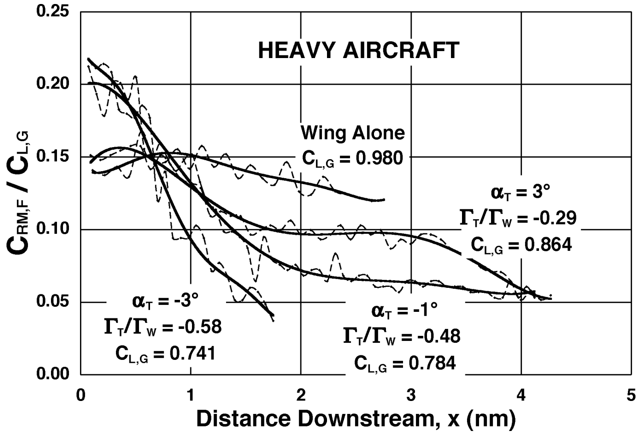

a) Heavy aircraft

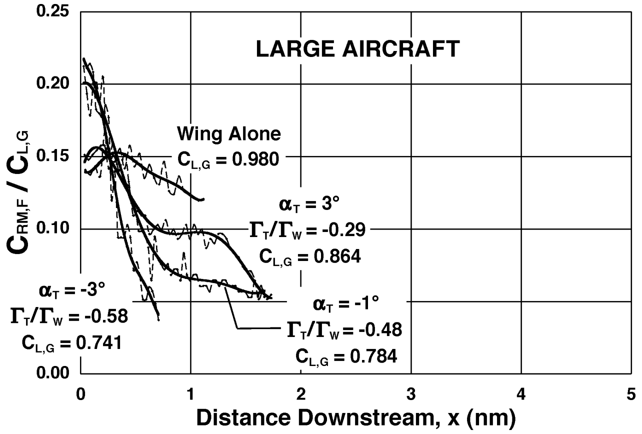

b) Large aircraft

Fig. 18 Following-wing rolling-moment decay with distance, wing-alone and 40%-span tail configurations; $\alpha_W = 8$ deg.

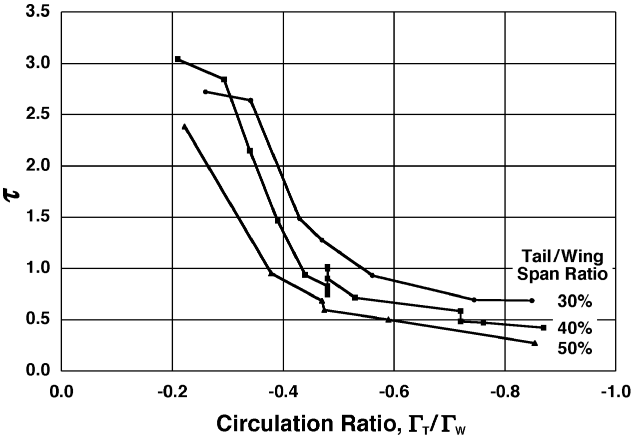

Fig. 19 Time to 50% decay in rolling moment with tail/wing circulation ratio.

The two plots in Fig. 18 show that the wake hazard persists more than twice as far (at any given wing-tail circulation ratio) for the heavy aircraft as it does for the large aircraft, which does not seem unreasonable considering the large difference in weight between the two. This also illustrates that the wake hazard problem will be much more difficult to solve for the heavy aircraft, in that relatively high induced rolling moments (for the −0.29-circulation-ratio case, for example) persisting for 3–4 nm downstream might not be enough of a hazard reduction to permit a tightening of the spacing much below the present 6 nm required for smaller aircraft following a heavy.

A figure of merit summarizing all of the rolling-moment data can be derived from noting the time by which the rolling moment is reduced by one-half. This does not imply anything about a particular aircraft's ability to survive an encounter with a wake that would induce such rolling moments, but it does allow the trends in the wake-vortex hazard reduction with tail span and circulation ratio to be clearly shown. This "time to half rolling moment," shown in Fig. 19, falls off rapidly as circulation ratios increase (in an absolute sense) from −0.2 to −0.5 for all tail spans, and then levels off from there to −0.85 circulation ratio. There is also a definite trend of reduction of this distance as tail span is increased, but it is clear that the primary driver for reducing the rolling moment quickly is the circulation ratio between the tail and the wing.

Note that the time-to-half rolling moment after the curves level off is in the range of $\tau = 0.5$ to 1 (approximately 50 to 80 wing spans for the configurations tested). For a 60-m (200-ft) span airplane, this corresponds to a distance of 1.6 to 2.6 nm. The U.S. separation standards for aircraft in trail range from 2.5 to 6 nm, depending on the leading- and following-aircraft categories, and so this degree of alleviation could have an impact on the separation standards if it could be achieved on every aircraft producing strong vortices. It is recognized, however, that this 50% reduction in induced rolling moment might not yet be enough to permit closer spacing while maintaining safety; greater reductions up to 75% might ultimately be required.

Alleviation is used in the context of this paper to mean that the wake is made safer (i.e., hazard reduced but not eliminated) for the given span and lift of the generating wing through the process of merging the wing and tail vortices. Granted, a single wing with a larger span can generate vortices of the same span and strength as the alleviated vortices from the wing-tail configuration, but the fact that the interaction of the two pairs of vortices results in a weakened vortex wake implies that the wake hazard has been somewhat alleviated for the given configuration relative to what it would have been without the vortex interactions. This alleviation is achieved by the reduced vortex strength, though it is recognized that vortices

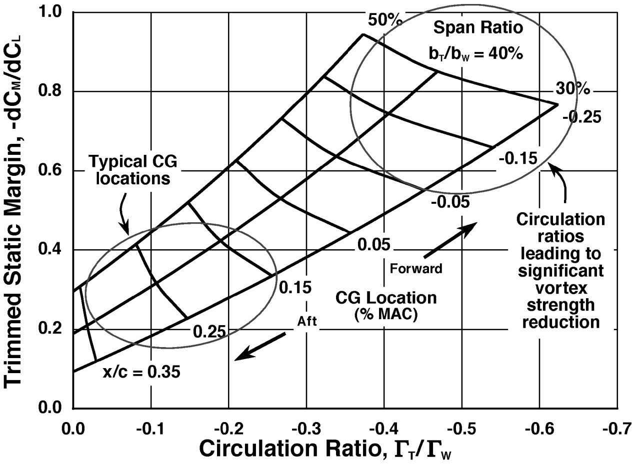

Fig. 20 Static margin vs circulation ratio for all three tail spans.

descending more slowly means that the reduced hazard remains near the likely flight path of following aircraft for a longer period of time.

Longitudinal Stability Analysis

Now that the circulation ratios required for a significant reduction in the rolling-moment hazard have been established for this wing-tail configuration, the question arises about how practical these ratios might be for real aircraft. High circulation ratios require high tail downloads, and, even though some download is typically required for trim on stable, conventional wing-tail aircraft, it is desired to keep it to a minimum within static longitudinal stability constraints because it opposes the wing lift. To assess the downloads required, a simple static stability analysis was performed to determine the static margins resulting from trimming the wing-tail configuration over the range of tail/wing circulation ratios of interest.

Longitudinal aerodynamic coefficients were estimated with LinAir for each of the configurations tested in the tow tank. Using data from a series of LinAir runs at various tail incidence angles, the angles required to trim the aerodynamic data for zero pitching moment were determined. Circulation ratios were estimated from the resulting trimmed lift using Eq. (2), and the static margins at these conditions were noted. The results are plotted in Fig. 20 and show that c.g. locations fairly far forward of the nominal wing quarter-chord location are required to achieve high circulation ratios. The plot also shows that the static margins for c.g. locations corresponding to circulation ratios greater than -0.40 would be 0.5 or higher, whereas most modern transport aircraft typically have static margins in the range of 15–40%. Flying with more forward c.g. locations would increase trim drag, reduce range, and increase operating costs, all of which would be penalties too substantial to pay to achieve some alleviation of the wake-vortex hazard. It would be convenient to be able to shift the c.g. forward just during the phases of flight when the hazard is the greatest, such as during landing approach, but fuel is usually the only heavy payload that can be moved around easily, and yet the range over which it can be moved is typically not very large, and even if it were, fuel is not usually plentiful just before landing.

Thus, this analysis has shown that flying with higher tail downloads to at least partially alleviate the wake-vortex hazard is not practical. However, this approach to alleviation—using counter-rotating vortices to achieve accelerated destruction of the wing vortices—can be made practical through the innovative use of aerodynamic devices or configuration changes that would generate counter-rotating vortices of sufficient strength.

Conclusions

A water tow tank study of the wake from a wing-tail configuration has been conducted to observe the vortex pair interactions over a wide range of circulation strength ratios. The vortex-strength-reduction behavior observed in University of California at Berkeley studies[11–13] with a triangular-flapped wing has been achieved with the wing-tail configuration, demonstrating that a conventional configuration with moderate-to-high tail downloads can generate similar wakes. These observations are also consistent with the results of Stuff[15,17] and Stuff and Vollmers,[16] and Stumpf[18] from their investigations of counter-rotating vortex pairs.

Particle image velocimetry has quantified the reduction in the induced rolling-moment hazard as a result of the vortex interactions. The extensive database of configurations tested has allowed the mapping of wing/tail circulation ratios and span ratios for which the vortex strength reduction occurs. The tests have also demonstrated some of the benefits of the interactions of counter-rotating vortex pairs, namely, that 1) vortex strength after merging is approximately the sum of the strengths of the two vortices, so that when they are of opposite signs the strength of the stronger one is diminished, and 2) the vorticity centroid is outboard of where it would be if the counter-rotating pair were not present.

However, a longitudinal stability analysis has identified the moderate-to-high static margins required to achieve the vortex strength reductions by the wing and tail vortex interactions alone. Although other vortex sources from an aircraft might contribute to these interactions in a positive or negative way (from an alleviation standpoint), the basic premise of carrying a substantial download on an aerodynamic surface to help alleviate a wake is fundamentally limited because of the lift and drag penalties incurred. Such high static margins are clearly impractical for most of today's transport aircraft, but it is hoped that some alternate configurations or aerodynamic devices—used passively or actively—might someday be found effective and practical enough for full-scale implementation.

A mechanism for accelerated vortex strength reduction has been confirmed (in the present work as well as in others'); a more practical way to exploit this mechanism is needed to put it into use.

Acknowledgments

The authors wish to express their appreciation to Vernon Rossow and Jason Ortega for the many discussions with them that have helped guide this research and identify that which is important to study.

References

[1] Bilanin, A. J., Teske, M. E., and Curtiss, H. C., Jr., "Feasibility of an Onboard Wake Vortex Avoidance System," NASA CR-17521, April 1987.

[2] O'Conner, C. J., and Rutishauser, D. K., "Enhanced Airport Capacity Through Safe, Dynamic Reductions in Aircraft Separation: NASA'S Aircraft VOrtex Spacing System (AVOSS)," NASA TM-2001-211052, Aug. 2001.

[3] Rossow, V. J., "Use of Individual Flight Corridors to Avoid Vortex Wakes," *Journal of Aircraft*, Vol. 40, No. 2, 2003, pp. 225–231.

[4] Rutishauser, D., Lohr, G., Hamilton, D., Powers, R., McKissick, B., and Adams, C., "Wake Vortex Advisory System (WakeVAS) Concept of Operations," NASA TM-2003-212176, April 2003.

[5] "Wake Vortex Minimization," NASA SP-409, 1977.

[6] Rossow, V. J., "Lift-Generated Vortex Wakes of Subsonic Transport Aircraft," *Progress in Aerospace Sciences*, Vol. 35, No. 6, 1999, pp. 507–660.

[7] Bilanin, A. J., and Quackenbush, T. R., "System and Method of Vortex Wake Control Using Vortex Leveraging," U.S. Patent 6,042,059, March 2000.

[8] Barber, M. R., and Tymczyszyn, J. J., "Wake Vortex Attenuation Flight Tests: A Status Report," NASA CP-2170, Part 2, 1981, pp. 387–408.

[9] Crouch, J. D., Miller, G. D., and Spalart, P. R., "Active-Control System for Breakup of Airplane Trailing Vortices," *AIAA Journal*, Vol. 39, No. 12, 2001, pp. 2374–2381.

[10] Loucel, R. E., and Crouch, J. D., "Flight-Simulator Study of Airplane Encounters with perturbed Trailing Vortices," AIAA Paper 2004-1074, Jan. 2004.

[11] Ortega, J. M., and Savaş, Ö., "Rapidly Growing Instability Mode in Trailing Multiple-Vortex Wakes," *AIAA Journal*, Vol. 39, No. 4, 2001, pp. 750–754.

[12] Ortega, J. M., Bristol, R. L., and Savaş, Ö., "Wake Alleviation Properties of Triangular-Flapped Wings," *AIAA Journal*, Vol. 40, No. 4, 2002, pp. 709–721.

[13] Ortega, J. M., Bristol, R. L., and Savaş, Ö., "Experimental Study of the Instability of Unequal-Strength Counter-Rotating Vortex Pairs," *Journal of Fluid Mechanics*, Vol. 474, Jan. 2003, pp. 35–84.

[14] Lourenço, L. M., and Krothapalli, A., "True Resolution PIV: A Mesh-Free Second Order Accurate Algorithm," *Proceedings of the 10th International Symposium on Application of Laser Techniques to Fluid Mechanics*, Calouste Gulbenkian Foundation, Lisbon, July 2000.

[15] Stuff, R., "The Near-Far Field Relationship of Vortices Shed from Transport Aircraft," AIAA Paper 2001-2429, June 2001.

[16] Stuff, R., and Vollmers, H., "Aircraft with Means for a Premature Breakdown of the Wing Vortex Pair," U.S. Patent 6,422,518, July 2002.

[17] Stuff, R., "Alleviation of Aircraft Vortex Hazard Through Passive Aerodynamic Measures," AIAA Paper 2003-1108, Jan. 2003.

[18] Stumpf, E., "Numerical Study of Four-Vortex Aircraft Wakes and Layout of Corresponding High-Lift Configurations," AIAA Paper 2004-1067, Jan. 2004.

[19] Durston, D. A., "LinAir: A Multi-Element Discrete Vortex Weissinger Aerodynamic Prediction Method," NASA TM-108786, Oct. 1993.